Publications of the Astronomical Society of Japan, 2025, **00**, 1–9
doi: 10.1093/pasj/xxx000
Advance access publication date:

The most completely sampled unified rotation curve of the Milky Way with the highest resolution and widest coverage

Yoshiaki SOFUE[1]

[1]Institute of Astronomy, The University of Tokyo, 2-21-1 Mitaka, Tokyo 181-8588, Japan
*E-mail: sofue@ioa.s.u-tokyo.ac.jp

ORCID: 0000-0002-4268-6499

Abstract

We update our unified rotation curve (URC) of the Milky Way (Sofue et al. 2009) to that with the highest spatial and velocity resolutions and the most complete sampling from the central supermassive black hole (SMBH) to the outermost dark halo, up to ~ 300 kpc; hence, it has the widest radial coverage. We present the curve in the form of figures and ascii tables. The URC can be ascribed to a combination of the following five components: 1. The central Keplerian curve due to the supermassive black hole at the nucleus; 2. a core component attributed to a high-density mass concentration within several parsecs of the Galactic Center, which can be fitted by a spherical mass concentration of scale radius and mass of ~ 2.4 pc and $\sim 3 \times 10^7 M_{\odot}$. 3. a bulge component with a high velocity peak at a radius of 0.4 kpc, which can be represented by a mass sphere of ~ 160 pc radius and $1.1 \times 10^{10} M_{\odot}$ or by an eccentric gas flow in the central bar. 4. a disk component that can be represented by an exponential disk with a scale radius and mass of ~ 3.8 kpc and $\sim 1.6 \times 10^{11} M_{\odot}$; and 5. an extended component that can be understood as being due to the dark halo, which can be fitted by the Navarro-Frenk-White type density distribution with a scale radius of $h \sim 14$ kpc and a density parameter $\rho_0 \sim 9 \times 10^{-3} M_{\odot}\ \mathrm{pc}^{3}$, with a critical radius and mass of $R_{200} \sim 81$ kpc and $M_{200}^{\rm total} \sim 4.2 \times 10^{11} M_{\odot}$. This dark halo yields the lower limit to the local DM density at the Sun of ~ 0.24 GeV cm^{-3}($\sim 6 \times 10^{-3} M_{\odot}\mathrm{pc}^{-3}$).

Keywords: galaxies: individual (Milky Way) — galaxies: kinematics and dynamics — Galaxy: kinematics and dynamics — Galaxy: structure — dark matter

1 Introduction

The rotation curve (RC) is the most fundamental tool for measuring the dynamical mass, including dark matter, and its distribution in galaxies under the assumption that a galaxy is rotating around the polar axis (Sofue and Rubin 2001; Sofue 2017; Sofue 2020; Lelli et al. 2016; McGaugh 2016; Salucci 2019). Photometry of luminous mass, e.g., stars, is a powerful tool to obtain the mass distribution in galaxies if a precise distribution of the mass-to-luminosity (M/L) ratio has already been prepared. However, for calculating the total mass, we need a dynamical determination of the mass because galaxies include dark matter.

This situation also applies exactly to the Milky Way Galaxy, whose rotation curve has been determined most precisely among the galaxies, and the mass distribution, including the dark halo, has been well determined (see Sofue (2020) and the wealth of literature therein). Extensive photometric determination, particularly in infrared wavelengths, has revealed the luminous mass distribution in the inner Galaxy and the detailed distribution of stellar components, including the nuclear disk, bulge and/or bar, and the inner disk (Schödel et al. 2014; Robin et al. 2012; Robin et al. 2014; Wegg et al. 2015; Portail et al. 2015; Ness & Lang 2016; Valenti et al. 2016; Simion et al. 2017; Marasco et al. 2025), while the dark matter mass, and hence the total mass, has been excluded from the photometric approach.

In our earlier papers (Sofue et al. 2009; Sofue 2012; Sofue 2013), we constructed a unified RC (URC) of the Galaxy from the nucleus to halfway to M31, including the outer halo, by combining the existing rotation data from the 1980s to the 2000s. We have also deconvolved the URC into several mass components to obtain fundamental parameters such as the total mass and scale size of each component, as well as the local density of dark matter (DM) (Sofue 2013; Sofue 2020).

In this paper, we revise the URC of the Milky Way by employing the most recent data about Galactic rotation and present a new unified rotation curve, which we call 'URC26'. We integrate the current RCs determined individually for the Galactic Center by the ALMA molecular line survey of the central molecular zone (CMZ) (Sofue et al. 2025), the inner disk using the CO and HI-line surveys of the Galactic plane (Sofue & Kohno 2025), the stellar disk by trigonometry of maser sources using VERA (VERA Collaboration et al. 2020) and VLBA (Reid et al. 2019), the disk stars by GAIA trigonometry (Eilers et al. 2019), and 3D velocities of globular clusters and dwarf galaxies with GAIA (Jiao et al. 2023; Sylos Labini 2024). However, we do not use the earlier RCs derived from HI and CO observations of the gas disk of the outer Galaxy outside the Solar circle, where the gaseous RC is claimed to be distinct from the stellar RC (Nelson et al. 2026). We adopt the Galactic constants $R_0 = 8.18$ kpc (Gravity Collaboration et al. 2019) and $\Theta_0 = 235.1\ \ \mathrm{km\,s^{-1}}$ (Sofue & Kohno 2025).

The main purpose of this paper is to construct the updated URC with the highest resolution, highest sampling, and widest radius coverage, and to present the curve in figures and tables for broader usage. As a byproduct, we try to deconvolve the URC into several mass components and calculate their masses and scale radii.

Received: , **Accepted:**

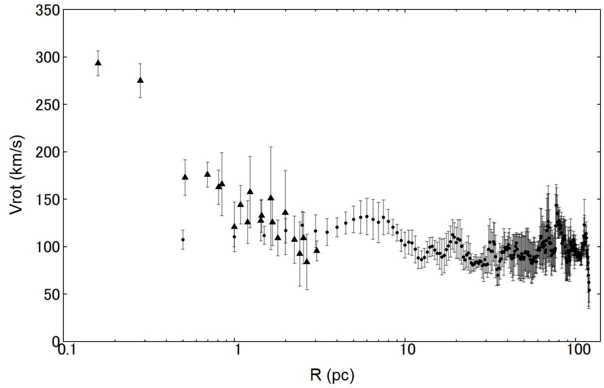

Fig. 1. Rotation curve of the CMZ in the central 120 pc obtained by terminal velocity method for H40α (triangles) and CS ($J=2-1$) (dots) lines in semilogarithmic scaling (Sofue et al. 2025). Alt text: Rotation curve of the Galactic Center.

2 Construction of a new URC

We integrate the partially determined rotation curves in specific radii based on the most recent observations. Below, we describe the data.

2.1 Central black hole

The rotation curve around the central supermassive black hole (SMBH) located at the nucleus (Sgr A*) with a mass of $M_1 = 4.0\times10^6 M_\odot$ (Ghez et al. 2008; Gillessen et al. 2009) is represented by the Keplerian law, as shown in figure 2 (A).

2.2 Central Molecular Zone (CMZ)

We have recently determined the RC in the CMZ using the ACES (ALMA CMZ Exploration Survey) data (Longmore et al. 2026; Ginsburg et al. 2025; Walker, D. L., et al. and ACES Team 2025; Lu et al. 2026; Hsieh et al. 2026; Battersby et al. 2026) by applying the terminal velocity method to the longitude-velocity diagrams (LVD) of the CS ($J=2-1$)-line emission from the molecular gas in the CMZ and the H40α-line from the ionized gas in the minispiral (Sofue et al. 2025). The entire CMZ has a nearly flat RC at $V_{\rm rot}\sim 100\ \ {\rm km\ s^{-1}}$ associated with a peak around $R\sim 5$ pc. The innermost $V_{\rm rot}$ within $R\lesssim 1$ pc increases toward the nucleus, obeying the Keplerian law due to the central SMBH.

2.3 Gas disk inside the solar circle by terminal velocities of CO and HI lines

Inside the solar circle ($-90^\circ \le l \le 90^\circ$), the rotation velocity $V(R)$ at the galacto-centric distance $R = R_0 \sin\, l$ is calculated simply by correcting the terminal velocity $V_{\rm term}$ for the circular motion of the LSR (local standard of rest) at the Sun:

$$V_{\rm rot}(R) = V_{\rm term} + \Theta_0\ \sin l. \qquad (1)$$

In figure 2 we show the inner RC obtained recently by Sofue & Kohno (2025), applying TVM to CO and HI line survey data of the Galactic plane (Dame et al. 2001; HI4PI Collaboration et al. 2016; Umemoto et al. 2017; Braiding et al. 2015; Cubuk et al. 2023), where the RCs from the literature described in the next two subsections are included by taking the running averages of all the available data.

2.4 Stellar disk by VLBI trigonometry of maser sources

Recent trigonometric measurements of maser sources using VERA (VLBI exploration of radio astrometry) (VERA Collaboration et al. 2020) and VLBA (very long baseline array) (Reid et al. 2019) have provided accurate 3D motions of the sources in the Galactic disk, which yielded rotation curves at high accuracy. These results were combined with the inner rotation curve from the terminal velocity to yield a rotation curve from the Galactic Center to the halo at $R\sim 15$ kpc. We include the rotation velocities of maser sources from VERA and VLBA measurements for the disk RC by taking running averages with our inner RC (Sofue & Kohno 2025). In this work, we do not use the gaseous rotation curve outside the Solar circle from CO and HI-line observations, which is claimed to be displaced from the Virial motion in the Galactic potential (Nelson et al. 2026).

2.5 Stellar disk and halo by GAIA trigonometry

The GAIA mission has provided proper motions of billions of stars in the Milky Way and yielded high accuracy rotation curves of the mid to outer Galactic disk at $R\sim 8$ to 25 kpc (Eilers et al. 2019; Jiao et al. 2023; Sylos Labini 2024). We also include their rotation curve by taking running averages with the RC for the disk described above.

2.6 Halo RC from 25 to 100 kpc by globular clusters

For the outer Galactic halo, we employ GAIA trigonometric measurements of globular clusters (Vasiliev & Baumgardt 2021; Wang et al. 2022). In figure 3 we plot the rotation velocities presented by Wang et al. (2022), which cover $R\sim 25$ to ~ 100 kpc.

2.7 Halo RC from 25 to 300 kpc by dwarf galaxies

For ~ 25 to 300 kpc we use the 3D velocities observed by the GAIA trigonometry of dwarf galaxies (Li et al. 2017; Li et al. 2021; Hammer et al. 2021; Hammer et al. 2023). Following Sofue (2013) we introduce a "pseudo" rotation velocity of dwarf galaxies defined by

$$V_{\rm rot} = \eta V_{\rm 3D} = \eta\sqrt{v_{\rm RA}^2 + v_{\rm Dec}^2 + v_{\rm radial}^2}. \qquad (2)$$

Here, v_i ($i=$ RA, Dec, radial) are the velocities calculated for the proper motions and radial velocity with GAIA, and η is a conversion factor for the 3D velocity to a pseudo circular velocity at the same radius. We assume $\eta\sim 1/\sqrt{2}$, considering that the dwarfs are halfway to their apocenters and the orbital inclinations to the line of sight are random. We also examine a case with $\eta=1$, which will yield the upper limit of the circular velocity. Using the velocities thus converted, we perform the Gaussian running average and plot them in figure 3. This "dwarf correction factor" η could vary between $\eta\sim 1$ and $\sim 1/\sqrt{3}$, depending on the dynamical condition of the halo. This means that the dark halo mass estimation in this paper includes a systematic error of a factor of ~ 2.

2.8 URC26: Unified RC from the GC to outermost halo

We then construct a unified RC (URC) by taking the Gaussian running average (GRA) of the rotation velocities $V(R_i)$ measured at $R=R_i$ for the i-th data points by the individual methods. The GRA value of V at a radius R is calculated by

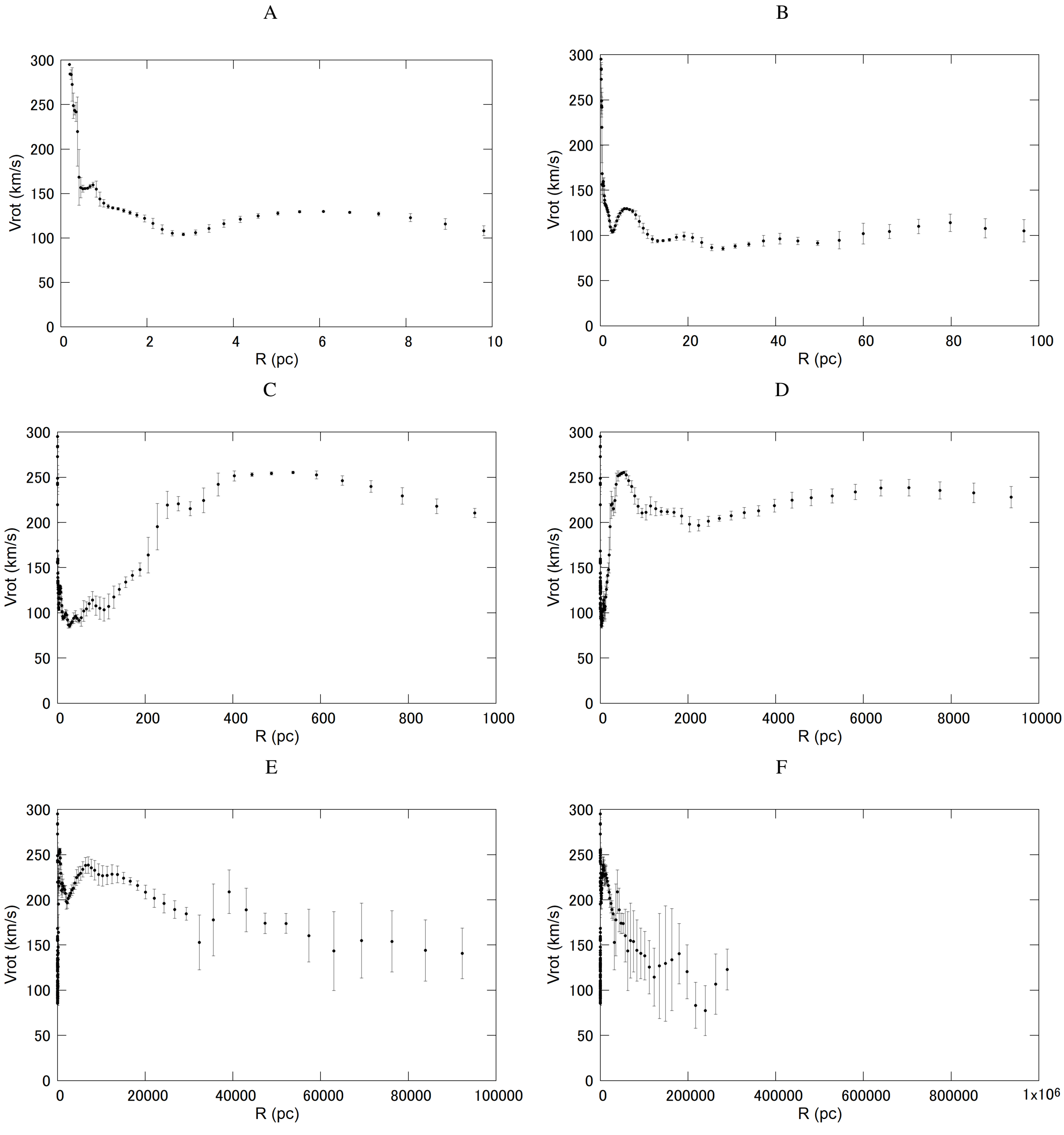

Fig. 2. [A] URC in the central 10 pc; [B] 0 to 100 pc; [C] 0 to 1 kpc; [D] 0 to 10 kpc; [E] 0 to 100 kpc; and [F] 0 to 1 Mpc. The URC was constructed by combining the innermost RC shown in figure 1, the inner RC of the gas disk using the terminal velocity method (black dots) (Sofue & Kohno 2025), trigonometry of maser sources with VERA (blue dots) (VERA Collaboration et al. 2020) and VLBA (magenta dots) (Reid et al. 2019), disk stars by GAIA DR3 (brown triangles) (Jiao et al. 2023), GAIA trigonometric rotation curves of globular clusters (Eadie & Jurić 2019; Vasiliev & Baumgardt 2021; Wang et al. 2022), and GAIA proper motions of dwarf galaxies for $\eta = 1/\sqrt{2}$ (Li et al. 2021; Hammer et al. 2021; Hammer et al. 2023). The innermost Keplerian curve represents the SMBH of $4 \times 10^6 M_\odot$ (Ghez et al. 2008). Alt text: URC26.

$$V(R) = \Sigma_{i=1}^{N} V_i w_i \;/\; \Sigma_{i=1}^{N} w_i \quad (3)$$

and

$$\delta V = \left[\Sigma (V(R) - V_i)^2 w_i \;/\; \Sigma w_i\right]^{1/2}, \quad (4)$$

where

$$w_i = \exp\left[-(R_i - R)^2 \;/\; \delta R^2\right] \sigma_i^{-2}, \quad (5)$$

and σ_i is the error of the observed value of the i-th data point, and $\delta R \sim 0.1R$ is the smoothing width. We plotted the URC in figure 3 at the same logarithmic radius interval and listed the calculated values in tables 2 — 5 in the appendix.

Figure 2 shows the obtained results with different scalings from the central region to the halo. Figure 3 shows a simultaneous plot of the RC that includes the SMBH, CMZ, bulge, disk, halo, and outer halo up to $\sim$ 300 kpc, about halfway to the Andromeda galaxy, in semi-logarithmic and logarithmic scaling. We name this RC the "URC26" (unified rotation curve 2026).

3 Approximate mass distribution

3.1 The major goal of this study

The major purpose of this paper was to present the newly constructed unified rotation curve of the Milky Way shown in figures 3 and 3, referred to as URC26. This rotation curve is sampled at the highest spatial resolution ever obtained, as well as the highest velocity resolution inside the solar circle, based on the accurate analysis of the highest resolution molecular line cube data of the Galactic disk using the terminal velocity method. It further combines the most recent proper motion data of globular clusters and dwarf galaxies. Thus, URC26 has achieved sufficiently tight logarithmic as well as semi-logarithmic plots of the rotation velocities, covering the widest area of the Galaxy from the central supermassive black hole to the dark matter halo at radii of approximately 300 kpc, almost halfway to the neighboring major member of the Local Group, M31. The curve is useful for a variety of analyzes of the Galactic structure and dynamics and the obtained valaues are listed in tables 2 – 5 in the Appendix.

3.2 Derivation of mass distribution

One of the important applications of rotation curves is the derivation of mass distribution, assuming circular rotation. However, this assumption is not fully plausible in the inner Milky Way, where a bar potential may controle the dynamics, and we will discuss the limitations and systematics of this method in section 4.2.1.

3.2.1 Basic method to derive the dynamical mass

We use the dynamical method based on the Virial theorem, which is a direct method using kinematical data such as the rotation curve. Widely adopted models to represent the bulge and disk are the exponential sphere, exponential disk, Sérsic type potential, Miyamoto-Nagai potential, and the Plummer potential. We adopt the exponential sphere for the core and bulge and a flat exponential disk for the disk component. We note that all these density models yield similar potentials due to the long range force of gravity, composed of a rigid-body rise, a peak at $\sim 2a$ (a =scale radii), and a Keplerian decrease, coinciding within a few percent. Note that $\exp(-x/a) = \exp(-x/2a)^2 \sim \mathrm{sech}(x/a) \sim \mathrm{sech}^2(x/2a)$, and $\mathrm{sech}^2(x/a^*)$ ($a^* = 2a$) is often used in other works. However, NFW type potentials for the dark halo behave quite differently, diverging outward because of the slow decrease in density.

3.2.2 Deconvolution into dynamical mass components

The rotation curve is represented by a superposition of N dynamical mass components as

$$V_{\mathrm{rot}}(R) = \sqrt{\Sigma_{i=1}^{N} V_i(R)^2}, \quad (6)$$

where $V_i(R)$ is the rotation velocity at radius R due to the i-th component. By closely examining URC26 in figure 4, we recognize five ($N = 5$) distinct mass components characterized by five velocity peaks at the center ($R \sim 0$ pc), $R \sim 5$ pc, ~ 500 pc, ~ 5000 pc, and an outskirt that extends to $R \sim 300$ kpc. We attribute these peaks to 1) SMBH, 2) core, 3) bulge, 4) disk, and 5) dark halo, and try to fit URC26 by superposing these mass components employing the following profiles. We then decompose the observed RC into the five components by the least-χ^2 method using the following functions representing the individual components. The fitted parameters are listed in table 1

3.2.3 Supermassive black hole

The innermost rotation curve at $R \lesssim 1$ pc is represented by the Keplerian law for the massive black hole with $M_{\mathrm{BH}} = 4 \times 10^6 M_\odot$ (Ghez et al. 2008; Gillessen et al. 2009):

$$\phi = GM_1/R, \quad (7)$$

and

$$V(R) = V_1/\sqrt{R/a_1} \quad (8)$$

with $V_1 = 131.5$ km s^{-1}and $a_1 = 1$ pc.

3.2.4 Core by an exponential sphere

For the core component, we adopt a spherical exponential density profile expressed as

$$\rho_i(R) = \rho_0^i \exp(-R/a_i), \quad (9)$$

where ρ_0^i and a_i are the central density and scale radius of the i-th mass component. The rotation velocity is calculated by

$$V_{\mathrm{rot}\,i}(R) = \sqrt{GM_i(R)/R}, \quad (10)$$

where

$$M_i(R) = \int_0^R \rho_i(r) 4\pi r^2 dr \quad (11)$$

is the enclosed mass inside R. We stress that, because gravity has a long range force, the exponential potential is a good approximation to that of a Plummer potential, as well as any similar mass concentrations with sufficiently rapid density decrease, with an accuracy of a few percent (Sofue 2017). By fitting to the URC, we obtain the scale radius and mass for the core to be $a_2 \simeq 2.4$ pc and $M_2 \simeq 3.3 \times 10^7 M_\odot$.

3.2.5 Bulge by an exponential sphere

We adopt the same form of the exponential sphere as the core expressed by equation 9. The fitting yields $a_3 \simeq 162$ pc and $M_3 \simeq 1.12 \times 10^{10} M_\odot$, which is nearly identical to the fit using the $\mathrm{sech}^2(R/a^*)$ function with $a_3^* \sim 2a_3 \sim 0.32$ kpc.

However, the inner Galaxy has a bar, and the bar-driven non-circular motion of the gas does not necessarily represent the true mass distribution. This issue will be discussed in a later section on the limitations and uncertainties of using the RC in this region.

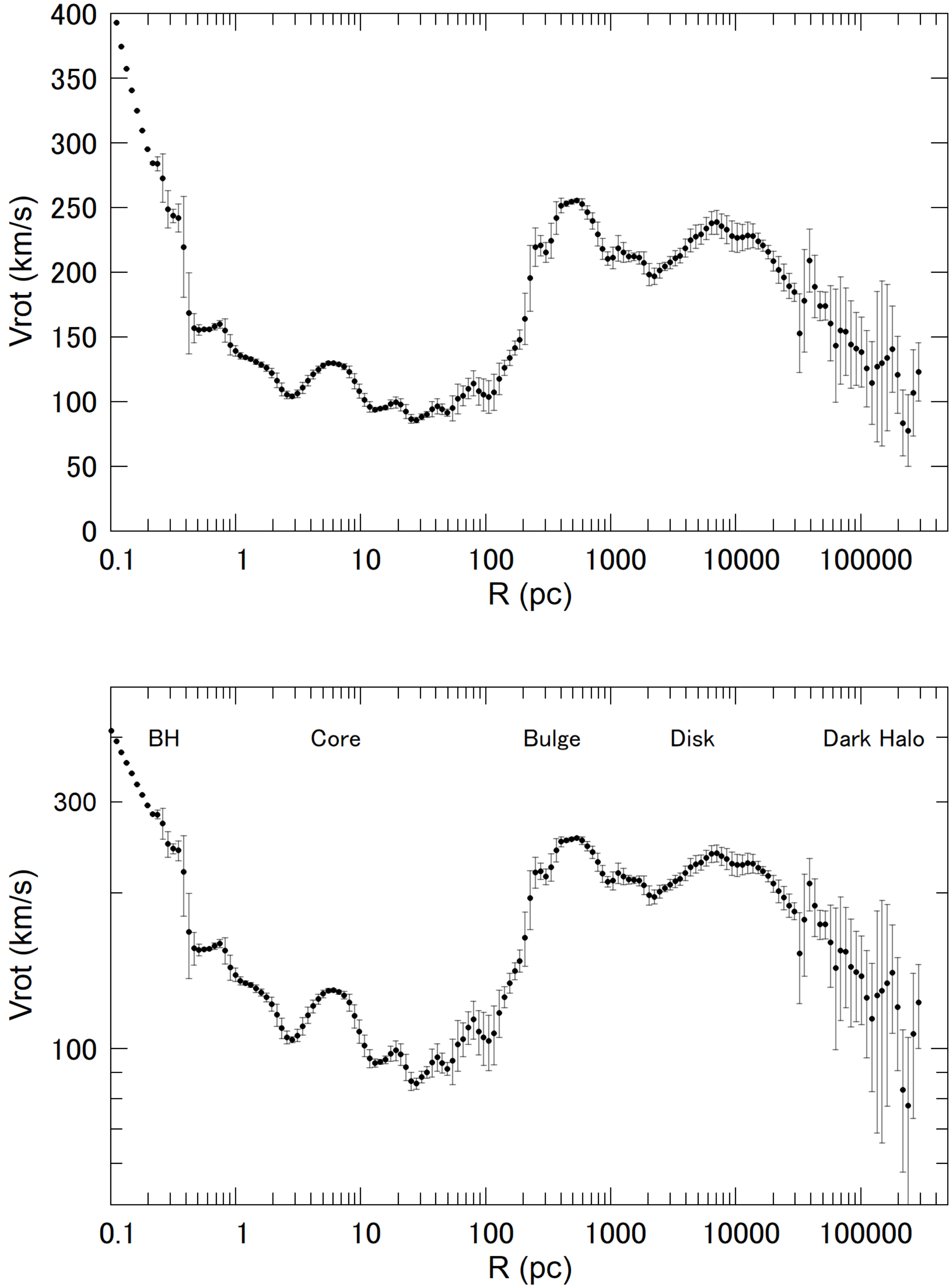

Fig. 3. [Top] URC2026 (same as figure 2) in semilogarithmic and [bottom] logarithmic scalings. We recognize five major components, which can be attributed to the SMBH (component 1), core (component 2), bulge (3), disk (4) and dark halo (5). The big dot marks the Sun at $(8.2\ \mathrm{kpc},\ 235\ \ \mathrm{km\,s^{-1}}\ )$.
Alt text: Unified rotation curve from the GC to halo.

3.2.6 Exponential disk

The galactic disk is represented by an exponential disk (Freeman 1970), where the surface mass density (SMD) is expressed as

$$\Sigma_4(R) = \Sigma_0 \exp(-R/a_4). \tag{12}$$

Here, Σ_0 is the central value, a_4 is the scale radius, and R is the radius inside the Galactic plane. The total mass of the exponential disk is given by $M_4 = 2\pi\Sigma_0 a_4^2$. The rotation velocity is expressed by

$$V_4(R) = V_0\sqrt{y^2[I_0(y)K_0(y) - I_1(y)K_1(y)]}, \tag{13}$$

where

$$V_0 = \sqrt{4\pi G\Sigma_0 a_4} = \sqrt{2GM_{\rm disk}/a_4} \tag{14}$$

or

$$M_4 = \frac{1}{2}\frac{a_4 V_0^2}{G}, \tag{15}$$

with $y = R/(2a_4)$, I_i, and K_i as the modified Bessel functions. By fitting, we obtain the disk radius and mass of $a_4 \simeq 3.8$ kpc and $M_4 \simeq 1.6\times10^{11} M_\odot$. The enclosed mass and local density are calculated using equation (12) assuming that the disk thickness is equal to the radius; hence, the calculated density is an approximate value.

3.2.7 Dark halo by NFW profile

The extended outskirts of the URC beyond $R \sim 15$ kpc can be fitted by the dark halo represented by the NFW (Navaro-Frenk-White) density profile (Navarro et al. 1997),

$$\rho_5(x) = \frac{\rho_0}{x(1+x)^2}, \tag{16}$$

where $x = R/h$ and $h = a_5$ are the scale radii. The rotation velocity is given by

$$V_{\rm rot\,5}(R) = \sqrt{GM_5(R)/R}, \tag{17}$$

and the mass inside R is given by

$$M_5(R) = 4\pi\rho_0 h^3[\ln(1+x) - x/(1+x)]. \tag{18}$$

By fitting, we obtain $h \sim 13.6$ kpc and $\rho_0 = 8.8\times10^{-3} M_\odot$ pc^{-3}. Combining these values with those obtained for the bulge and disk and referring to URC26, as shown in figure 5, we obtain the critical radius and mass of the Galaxy to be $R_{200} \sim 80$ kpc at which the mass density becomes equal to the cosmological critical density, $\rho_{200} = 200\times(3H_0^2)/(8\pi G) = 1.9\times10^{-27}$g cm^{-3} = $2.8\times10^{-5} M_\odot$pc^{-3} with $H_0 = 71$ km s^{-1}Mpc^{-1} being the Hubble constant. The critical mass is obtained as $M_{200} = M(R_{200}) \sim 4\times10^{11} M_\odot$.

3.2.8 Mass and density distributions

The least χ^2 fitting results using these functions are summarized in table 1. The rotation velocity was calculated using the fitted parameters and plotted in Figure 4. The calculated RC reproduces URC26 from the center to $R \sim 30$ kpc well, and the outer halo (up to 300 kpc) also shows a reasonable fit within the margin of error. URC26 demonstrates the existence of a massive halo in the outermost region up to $R \sim 300$ kpc, which can be reasonably represented by the NFW mass model. However, URC26 does not support the Keplerian decrease in rotation velocity at $R \gtrsim 25$ kpc.

Using dynamically fitted parameters, the density distribution and cumulative mass were calculated as a function of R and plotted in Figure 5. This diagram shows that mass is concentrated at a high density over a range of more than 10 orders of magnitude, from the dark halo to the nucleus.

Table 1. Fitting parameters of the URC26 for $\eta = 1/\sqrt{2}$.

i-th component	Parameter
1. SMBH	$M_1 \simeq 4.0\times10^6 M_\odot$ ‡
2. Core	$a_2 \simeq 2.44\pm0.03$ pc $M_2 \simeq (3.33\pm0.06)\times10^7 M_\odot$
3. Bulge	$a_3 \simeq 162\pm1.3$ pc $M_3 \simeq (1.12\pm0.01)\times10^{10} M_\odot$
4. Disk	$a_4 \simeq 3.82\pm0.06$ kpc $M_4 \simeq (1.66\pm0.04)\times10^{11} M_\odot$
5. Dark halo	$4\pi\rho_0 h^3 \sim (2.78\pm0.08)\times10^{11} M_\odot$ $\rho_0 = (8.82\pm0.25)\times10^{-3} M_\odot{\rm pc}^{-3}$ $a_5 = h \simeq 13.6\pm0.5$ pc $R_{200} \sim 81$ kpc $M_{200} \sim 4.2\times10^{11} M_\odot$

‡ Ghez et al. (2008)

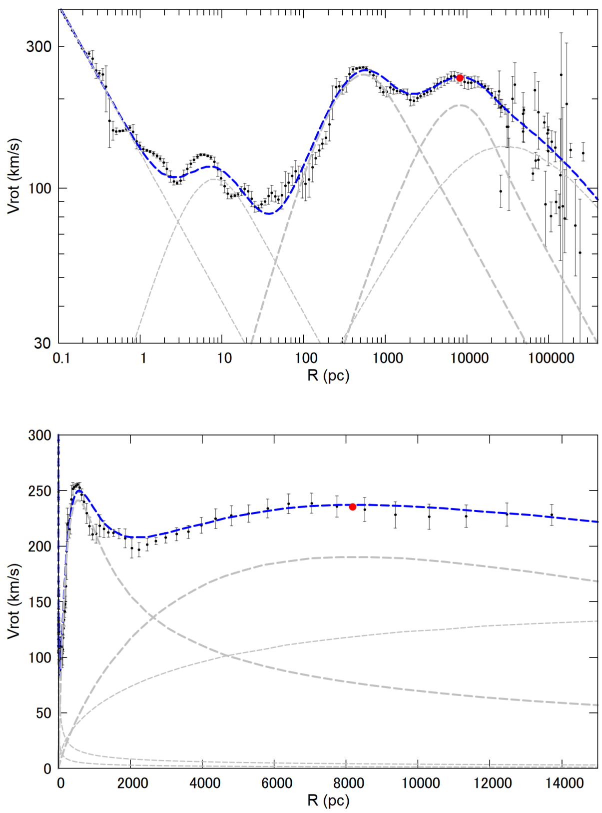

Fig. 4. Decomposition of the URC by five mass components for the parameters given in table 1. [Top] Logarithmic URC from the nucleus to outer halo. [Bottom] Same, but in linear scaling. Alt text: Dynamical decomposition of URC.

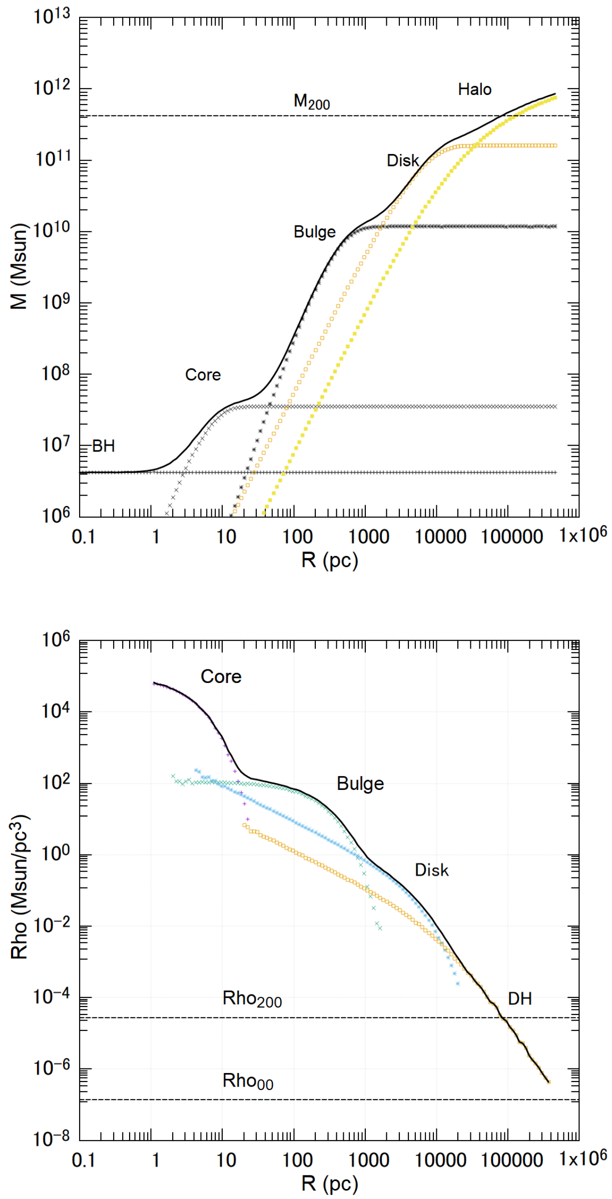

Fig. 5. [Top] Cumulative mass $M(R)$ calculated for the observed values of rotation velocity $\eta = 1/\sqrt{2}$ (dots) and least-χ^2 fitted URC for the core, bulge and disk. [Bottom] Volume density calculated for the fitted URC in the top panel. Alt text: Cumulative mass and density distributions.

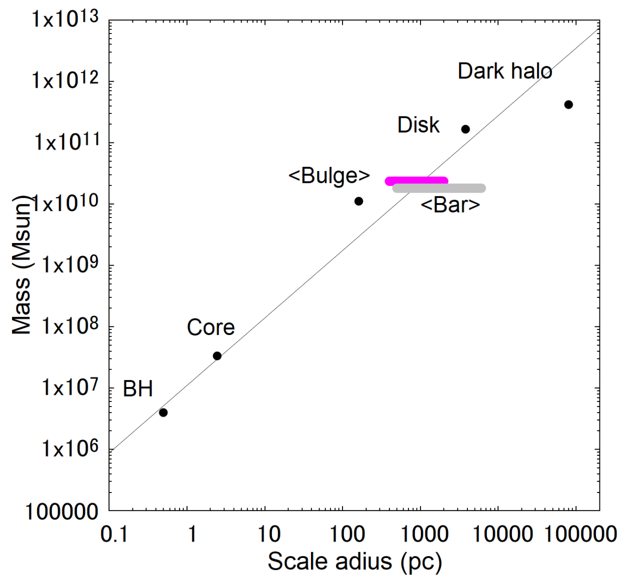

Fig. 6. Scale radius vs total mass of the five mass components of the Milky Way. The radius for BH is approximated by its 'gravity dominant radius'. Instead of the bulge, we may adopt photometric bar (Simion et al. 2017) (magenta thick line) or a dynamical model (Hunter et al. 2024) (grey thick line). The DH represent $M_{200}^{\rm DM}$ (DH component alone). The thin straight line indicates $M = 10^7 (R/1{\rm pc})^{1.1} M_\odot$. Alt text: Scaling relation among the deconvolved mass components.

3.2.9 Local DM density

The local density of DM is a key parameter for the direct detection experiments of DM. Using figure 5 (equation 16) we obtain the local density of DM at the Sun due to the dark halo alone to be $\rho_\odot^{\rm DM} \sim 6.2 \times 10^{-3} M_\odot {\rm pc}^{-3} \simeq 0.24$ GeV cm^{-3} . Note that this value represents only the dark halo contribution, not including the DM in the disk and bulge. So, this is a lower limit of the DM density near the Sun.

3.3 Scaling relation

Deconvolution of the URC into multiple components enables us to examine the scaling relation between the scale radius, a_i, and total mass, M_i, among the SMBH, core, bulge, disk, and dark halo. For the BH, we define the scale radius as the radius at which the gravity of the BH dominates that of the core component, i.e., $a_{\rm BH} \sim 0.5$ pc. Figure 6 shows the total masses thus derived against the scale radii of the five components. We find a linear proportionality between the radius and the total mass, which varies by more than six orders of magnitude and is expressed by $M \sim 10^7 M_\odot (R/1~{\rm pc})^{1.1}$, as shown by the straight line in the figure. The diagram may provide a scaling relation within an individual galaxy about the co-evolution of the BH, bulge, disk, and dark halo. This provides a complementary relation to the scaling law between the masses of the BHs and bulges among different galaxies (Kormendy & Ho 2013).

4 Discussion

4.1 Consistency with mass determinations by photometric observations

Extensive photometric observations in infrared wavelengths at ~ 2 to $\sim 4\mu$m have been obtained of the central stellar component (Schödel et al. 2014), the bulge, and the inner disk (Robin et al. 2012; Robin et al. 2014; Wegg et al. 2015; Portail et al. 2015; Ness & Lang 2016; Valenti et al. 2016; Simion et al. 2017; Marasco et al. 2025). Our results for the scale radii and masses of the core, bulge, and disk are consistent with these results within a factor of 1.5 to 2, as described below.

However, the 3D structure of the bar inferred from the photometric study for the bulge cannot be directly compared with our rotation curve study because our rotation curve provides the averaged circular speed as a function of R alone. See the next subsection about the implications of the RC for the bar study.

4.1.1 Core

The photometric scale radius and mass of the central stellar cluster, $a_2 \simeq 4.1$ pc and $M_2 \sim 4.2 \times 10^7 M_\odot$, from the infrared photometry (Schödel et al. 2014) are close to the dynamical values in table 1, and the resulting rotation velocity is consistent with one another.

4.1.2 Bulge

The scale radius of the central bulge or a bar inferred from infrared photometry of $a_3^* \sim 2a_3 \sim 0.4-2$ kpc (Simion et al. 2017) is larger than the dynamical fitting value of $2a_3 = a_3^* \sim 0.3$ kpc. The photometric mass $\sim 1.8-2.4 \times 10^{10} M_\odot$ is also about twice the dynamical mass of $M_3 \sim 1.1 \times 10^{10} M_\odot$. However, the photometry lacks observations of the brightest region in the galactic plane at $|b| \lesssim 1^\circ.5 \sim 200$ pc due to heavy dust extinction (Simion et al. 2017), hence the major body of the bar is not observed. So, the assumed $\mathrm{sech}^2(R/a_3^*)$ density profile, along with parameter values, needs to be confirmed by future observations near the galactic plane.

4.1.3 Disk

The photometric scale radius of the disk of $a_4 \simeq 2.4$ kpc (Robin et al. 2014) is within an allowable range of agreement with the present dynamical fitting value of 3.8 kpc. However, the total disk mass is not given by photometry because it cannot detect the disk edge far beyond the solar circle.

4.1.4 Dark halo

There seems to be no way to measure dark halo mass without employing the Virial theorem using rotation curves and/or the velocity dispersion of the halo objects. Therefore, the present fitting using the rotation curve up to ~ 300 kpc may be a powerful means to measure the dark halo currently.

4.2 Implications of URC on the Galactic dynamics

4.2.1 Limitation of RC usage

The rotation curve is defined as the mean circular velocity of gas and stars in the galactic plane as a one dimensional function of the radius R, where non-circular or non-axisymmetric properties, such as the east-west asymmetry of the terminal velocities with respect to the Galactic Center, have been averaged out. On this basis, we have obtained the approximate mass distribution in the Galaxy by deconvolving the curve into the five dynamical components, from the SMBC to the dark halo. Since it is a one variable function of R, a rotation curve cannot be used to directly calculate higher-order mass distributions, such as those due to a bar and spiral arms. Considering the effects of bar and spiral structures, there is a limitation on the use of the rotation curve, whereas it may assist in modeling the inner bar structure.

4.2.2 Bar-induced non-axisymmetric flows

Evidence has accumulated that Galactic rotation contains non-axisymmetric components, with the amplitude depending on the galacto-centric distance. GAIA trigonometry revealed systematic non-circular motions of OB stars at $V_\phi - V_0 \sim \pm 5\ \mathrm{km\,s^{-1}}$ in the Solar vicinity within ~ 2 kpc ($6.5 \lesssim R \lesssim 10$ kpc) due to the spiral arms (Gaia Collaboration et al. 2023). Since these motions of the arms are smaller than the errors of the present URC of $\sim \pm 10\ \mathrm{km\,s^{-1}}$ (table 4) and are considered to be periodic (sinusoidal) from arm to arm, the URC made from azimuthally averaged motions may be regarded as representing the circular motion within the errors attached in the table.

Eastern and western (positive and negative longitudes) asymmetry of the inner rotation curve at $R \lesssim 5$ kpc has long been known and is considered evidence of non-circular motion caused by a bar and/or spiral arms (Manabe & Miyamoto 1975; Liszt & Burton 1980; Sofue & Kohno 2025). Our high-accuracy measurement of the terminal velocities of the CO and HI gas disks has revealed an east-to-west asymmetry at $R \lesssim 6\ \mathrm{km\,s^{-1}}$ with the amplitude of $\sim 20\ \mathrm{km\,s^{-1}}$ sinusoidally oscillating against R (Sofue & Kohno 2025). A bar-induced eccentric flow has been more directly observed through the VLBI trigonometry of high-mass star masers, which has shown significant systematic non-circular motions of $\sim 30-50\ \mathrm{km\,s^{-1}}$ near the Galactic bar end at $R \sim 5$ kpc ($3 \lesssim R \lesssim 5$ kpc) (Reid et al. 2019).

Given such a bar structure, the RC inside the central few kpc needs to be interpreted more carefully to see whether it explicitly reflects the dynamical mass or is affected by the eccentric motions, so that the RC derived value of the mass is under- or over-estimated compared to the true mass. Further discussion of a bar is beyond the scope of this paper, but a simulation-based study could be a possible tool to obtain the truth.

4.2.3 Constraints on theoretical models

From the theoretical side, it is known that the bar-induced eccentric motion results in either an over- or under-estimation of the mass depending on the bar's position angle and pattern speed (Sorensen et al. 1976; Binney et al. 1991; Sormani et al. 2015a; Sormani et al. 2015b). Namely, bars with the same mass but different orientations yield different amplitudes and radii of the RC peak (Liu et al. 2025). In our Galaxy, this effect is typically observed as the high-velocity peak of the RC at $R \sim 0.4$ kpc.

Numerical simulations have shown that this RC peak can be explained by the streaming motion of gas in a nearly head-on bar (Chemin et al. 2015; Hunter et al. 2024; Sormani et al. 2015a; Sormani et al. 2015b). Therefore, the currently fitted bulge may not accurately reflect the actual mass structure. Conversely, the most accurate URC presented in this paper, along with the well quantified E/W sinusoidal variation of the terminal velocity (Sofue & Kohno 2025), can be used to validate the simulation results and constrain the parameters for the underlying mass model, including the bar's shape and mass distribution.

5 Summary

We derived the most completely sampled unified rotation curve of the Milky Way (URC26), covering the widest radius from the central supermassive black hole to the outer halo of radius ~ 300 kpc, which has the highest resolution and accuracy ever achieved for a galaxy. The URC was decomposed into five dynamical components: the central black hole with a mass of $M_1 = 4 \times 10^6 M_{\odot}$, the core with $M_2 \simeq 3.3 \times 10^7 M_{\odot}$ (core), the bulge with $M_3 \simeq 1.1 \times 10^{10} M_{\odot}$ (bulge), the disk with $M_4 \simeq 1.6 \times 10^{11} M_{\odot}$ (disk), and the dark halo with a critical mass of $M_{200} \sim 4.2 \times 10^{11} M_{\odot}$ in the critical radius $R_{200} \sim 81$ kpc. The local dark matter density near the Sun, due to the dark halo alone, is estimated to be $\rho_{\odot}^{\rm DM} \sim 0.24$ GeV cm^{-3} . We found a linear proportionality between the scale radius and the mass of the individual components.

Acknowledgments

Data analysis was performed at the NAOJ Astronomy Data Center. This work was supported by Kakenhi No. JP24H00004 of MEXT Japan.

Conflict of interests

The author declares that there are no conflicts of interest.

Data availability

The rotation curve used in this paper is downloadable from the PASJ supplementary site at "http: (to be given by PASJ)" .

References

Battersby, C., Santa-Maria, M. G., Lipman, D., et al. 2026, arXiv:2602.20262.
Binney, J., Gerhard, O. E., Stark, A. A., et al. 1991, MNRAS, 252, 210.
Braiding, C., Burton, M. G., Blackwell, R., et al. 2015, PASA, 32, e020.
Chemin, L., Renaud, F., & Soubiran, C. 2015, A&A, 578, A14.
Cubuk, K. O., Burton, M. G., Braiding, C., et al. 2023, PASA, 40, e047.
Dame, T. M., Hartmann, D., & Thaddeus, P. 2001, ApJ, 547, 2, 792.
Eadie, G. & Jurić, M. 2019, ApJ, 875, 2, 159.
Eilers, A.-C., Hogg, D. W., Rix, H.-W., et al. 2019, ApJ, 871, 1, 120.
Freeman, K.C. On the Disks of Spiral and S0 Galaxies. Astrophys. J. 1970, 160, 811.
Gaia Collaboration, Drimmel, R., Romero-Gómez, M., et al. 2023, A&A, 674, A37.
Ghez, A.M.; Salim, S.; Weinberg, N.N.; et al.ApJ 2008, 689, 1044.
Gillessen, S.; Eisenhauer, F.; Trippe, S.; Alexander, T.; Genzel, R.; Martins, F.; Ott, T. ApJ 2009, 692, 1075.
Ginsburg, A., et al. submitted to MNRAS.
Gravity Collaboration, Abuter, R., Amorim, A., et al. 2019, A&A, 625, L10.
Hammer, F., Wang, J., Pawlowski, M. S., et al. 2021, ApJ, 922, 2, 93.
Hammer, F., Li, H., Mamon, G. A., et al. 2023, MNRAS, 519, 4, 5059.
Hsieh, P.-Y., Walker, D. L., Ginsburg, A., et al. 2026, arXiv:2603.00863.
HI4PI Collaboration, Ben Bekhti, N., Flöer, L., et al. 2016, A&A, 594, A116.
Hunter, G. H., Sormani, M. C., Beckmann, J. P., et al. 2024, A&A, 692, A216.
Jiao, Y., Hammer, F., Wang, H., et al. 2023, A&A, 678, A208.
Kormendy, J. & Ho, L. C. 2013, ARA&A, 51, 1, 511.
Lelli, F., McGaugh, S. S., & Schombert, J. M. 2016, AJ, 152, 6, 157.
Li, Z.-Z.; Jing, Y.P.; Qian, Y.-Z.; Yuan, Z.; Zhao, D.-H. ApJ 2017, 850, 116.
Li, H., Hammer, F., Babusiaux, C., et al. 2021, ApJ, 916, 1, 8.
Liu, J., Li, Z., & Shen, J. 2025, ApJ, 980, 1, 146.
Liszt, H. S. & Burton, W. B. 1980, ApJ, 236, 779.
Longmore, S. N., Bally, J., Barnes, A. T., et al. 2026, arXiv:2602.20340.
Lu, X., Walker, D. L., Ginsburg, A., et al. 2026, arXiv:2602.20445.
McGaugh, S. S. 2016, ApJ, 816, 1, 42.
Manabe, S. & Miyamoto, M. 1975, PASJ, 27, 1, 35.
Marasco, A., Fall, S. M., Di Teodoro, E. M., et al. 2025, A&A, 695, L23.
Miyamoto, M. & Nagai, R. 1975, PASJ, 27, 533.
Navarro, J.F.; Frenk, C.S.; White, S.D.M.ApJ. 1997, 490, 493.
Nelson, A. H., Sofue, Y., & Williams, P. R. 2026, arXiv:2606.11872.
Ness, M. & Lang, D. 2016, AJ, 152, 1, 14.
Poggiani, R. 2025, Galaxies, 13, 3, 65.
Portail, M., Wegg, C., Gerhard, O., et al. 2015, MNRAS, 448, 1, 713.
Reid, M. J., Menten, K. M., Brunthaler, A., et al. 2019, ApJ, 885, 2, 131.
Robin, A. C., Marshall, D. J., Schultheis, M., et al. 2012, A&A, 538, A106.
Robin, A. C., Reylé, C., Fliri, J., et al. 2014, A&A, 569, A13.
Salucci, P.A&Ap. Rev. 2019, 27, 2.
Schödel, R., Feldmeier, A., Kunneriath, D., et al. 2014, A&A, 566, A47.
Simion, I. T., Belokurov, V., Irwin, M., et al. 2017, MNRAS, 471, 4, 4323.
Söding, L., Bartel, R. L., & Mertsch, P. 2025, MNRAS, 542, 4, 2987.
Sofue, Y. 2012, PASJ, 64, 75.
Sofue, Y. PASJ 2013, 65, 118.
Sofue, Y.PASJ 2017, 69, R1.
Sofue, Y. 2020, Galaxies, 8, 37.
Sofue, Y.; Honma, M.; Omodaka, T. PASJ 2009, 61, 227.
Sofue, Y. & Kohno, M. 2025, PASJ, 77, 6, 1335.
Sofue, Y., Oka, T., Longmore, S. N., et al. 2025, arXiv:2504.03331.
Sofue, Y.; Rubin, V.ARA&Ap 2001, 39, 137.
Sorensen, S.-A., Matsuda, T., & Fujimoto, M. 1976, Ap&SS, 43, 2, 491.
Sormani, M. C., Binney, J., & Magorrian, J. 2015, MNRAS, 449, 3, 2421. doi:10.1093/mnras/stv441
Sormani, M. C., Binney, J., & Magorrian, J. 2015, MNRAS, 454, 2, 1818. doi:10.1093/mnras/stv2067
Sylos Labini, F. 2024, ApJ, 976, 2, 185.
Umemoto, T., Minamidani, T., Kuno, N., et al. 2017, PASJ, 69, 78
Valenti, E., Zoccali, M., Gonzalez, O. A., et al. 2016, A&A, 587, L6.
VERA Collaboration, Hirota, T., Nagayama, T., et al. 2020, PASJ, 72, 4, 50.
Walker, D. L., et al. 2025, submitted to MNRAS
Wegg, C., Gerhard, O., & Portail, M. 2015, MNRAS, 450, 4, 4050.
Vasiliev, E. & Baumgardt, H. 2021, MNRAS, 505, 4, 5978.
Wang, J., Hammer, F., & Yang, Y. 2022, MNRAS, 510, 2, 2242.
White, M. 2001, A&A, 367, 27.

Appendix 1 Table of the URC26

In this appendix, we present the URC26 in the form of ASCII tables in tables 2 — 5.

Table 2. URC26

R (pc)	$V_{\rm rot}$ (km s^{-1})	$\delta V_{\rm rot}$ (km s^{-1})
0.200E-01	0.926E+03	0.000E+00
0.220E-01	0.883E+03	0.000E+00
0.242E-01	0.842E+03	0.000E+00
0.266E-01	0.803E+03	0.000E+00
0.293E-01	0.766E+03	0.000E+00
0.322E-01	0.730E+03	0.000E+00
0.354E-01	0.696E+03	0.000E+00
0.390E-01	0.664E+03	0.000E+00
0.429E-01	0.633E+03	0.000E+00
0.472E-01	0.603E+03	0.000E+00
0.519E-01	0.575E+03	0.000E+00
0.571E-01	0.548E+03	0.000E+00
0.628E-01	0.523E+03	0.000E+00
0.690E-01	0.499E+03	0.000E+00
0.759E-01	0.475E+03	0.000E+00
0.835E-01	0.453E+03	0.000E+00
0.919E-01	0.432E+03	0.000E+00
0.101E+00	0.412E+03	0.000E+00
0.111E+00	0.393E+03	0.000E+00
0.122E+00	0.375E+03	0.000E+00
0.135E+00	0.357E+03	0.000E+00
0.148E+00	0.341E+03	0.000E+00
0.163E+00	0.325E+03	0.000E+00
0.179E+00	0.310E+03	0.000E+00
0.197E+00	0.295E+03	0.000E+00
0.217E+00	0.284E+03	0.100E+01
0.238E+00	0.284E+03	0.544E+01
0.262E+00	0.273E+03	0.187E+02
0.288E+00	0.249E+03	0.143E+02
0.317E+00	0.244E+03	0.521E+01
0.349E+00	0.242E+03	0.107E+02
0.384E+00	0.220E+03	0.389E+02
0.422E+00	0.168E+03	0.314E+02
0.465E+00	0.157E+03	0.114E+02
0.511E+00	0.155E+03	0.398E+01
0.562E+00	0.156E+03	0.100E+01
0.618E+00	0.156E+03	0.920E+00
0.680E+00	0.158E+03	0.235E+01
0.748E+00	0.160E+03	0.291E+01
0.823E+00	0.155E+03	0.912E+01
0.905E+00	0.144E+03	0.793E+01
0.996E+00	0.139E+03	0.413E+01
0.110E+01	0.135E+03	0.246E+01
0.120E+01	0.134E+03	0.119E+01
0.133E+01	0.133E+03	0.129E+01
0.146E+01	0.131E+03	0.206E+01
0.160E+01	0.128E+03	0.199E+01
0.176E+01	0.126E+03	0.245E+01
0.194E+01	0.122E+03	0.382E+01
0.213E+01	0.116E+03	0.573E+01
0.235E+01	0.110E+03	0.498E+01
0.258E+01	0.105E+03	0.291E+01
0.284E+01	0.104E+03	0.145E+01
0.312E+01	0.106E+03	0.288E+01

Table 3. URC26: continued

R (pc)	$V_{\rm rot}$ (km s^{-1})	$\delta V_{\rm rot}$ (km s^{-1})
0.344E+01	0.111E+03	0.431E+01
0.378E+01	0.116E+03	0.423E+01
0.416E+01	0.121E+03	0.344E+01
0.458E+01	0.125E+03	0.277E+01
0.503E+01	0.128E+03	0.211E+01
0.554E+01	0.130E+03	0.120E+01
0.609E+01	0.130E+03	0.780E+00
0.670E+01	0.129E+03	0.103E+01
0.737E+01	0.127E+03	0.210E+01
0.811E+01	0.123E+03	0.456E+01
0.892E+01	0.116E+03	0.607E+01
0.981E+01	0.108E+03	0.551E+01
0.108E+02	0.101E+03	0.492E+01
0.119E+02	0.958E+02	0.384E+01
0.131E+02	0.938E+02	0.176E+01
0.144E+02	0.944E+02	0.100E+01
0.158E+02	0.952E+02	0.153E+01
0.174E+02	0.979E+02	0.342E+01
0.191E+02	0.992E+02	0.434E+01
0.210E+02	0.975E+02	0.475E+01
0.231E+02	0.921E+02	0.541E+01
0.254E+02	0.866E+02	0.352E+01
0.280E+02	0.857E+02	0.211E+01
0.308E+02	0.882E+02	0.231E+01
0.339E+02	0.901E+02	0.232E+01
0.372E+02	0.941E+02	0.581E+01
0.410E+02	0.964E+02	0.583E+01
0.451E+02	0.939E+02	0.409E+01
0.496E+02	0.915E+02	0.265E+01
0.545E+02	0.947E+02	0.956E+01
0.600E+02	0.102E+03	0.115E+02
0.660E+02	0.104E+03	0.784E+01
0.726E+02	0.110E+03	0.786E+01
0.798E+02	0.114E+03	0.961E+01
0.878E+02	0.108E+03	0.107E+02
0.966E+02	0.105E+03	0.124E+02
0.106E+03	0.103E+03	0.127E+02
0.117E+03	0.107E+03	0.139E+02
0.129E+03	0.117E+03	0.123E+02
0.141E+03	0.126E+03	0.593E+01
0.156E+03	0.134E+03	0.588E+01
0.171E+03	0.141E+03	0.537E+01
0.188E+03	0.148E+03	0.729E+01
0.207E+03	0.164E+03	0.197E+02
0.228E+03	0.195E+03	0.255E+02
0.251E+03	0.219E+03	0.150E+02
0.276E+03	0.221E+03	0.790E+01
0.303E+03	0.215E+03	0.765E+01
0.333E+03	0.224E+03	0.136E+02
0.367E+03	0.242E+03	0.126E+02
0.404E+03	0.251E+03	0.560E+01
0.444E+03	0.253E+03	0.193E+01
0.488E+03	0.254E+03	0.169E+01
0.537E+03	0.255E+03	0.140E+01
0.591E+03	0.253E+03	0.432E+01

Table 4. URC26: continued

R (pc)	$V_{\rm rot}$ (km s^{-1})	$\delta V_{\rm rot}$ (km s^{-1})
0.650E+03	0.246E+03	0.527E+01
0.715E+03	0.240E+03	0.633E+01
0.786E+03	0.229E+03	0.908E+01
0.865E+03	0.218E+03	0.803E+01
0.951E+03	0.211E+03	0.502E+01
0.105E+04	0.211E+03	0.836E+01
0.115E+04	0.218E+03	0.994E+01
0.127E+04	0.215E+03	0.769E+01
0.139E+04	0.212E+03	0.418E+01
0.153E+04	0.212E+03	0.303E+01
0.169E+04	0.211E+03	0.468E+01
0.185E+04	0.207E+03	0.856E+01
0.204E+04	0.198E+03	0.857E+01
0.224E+04	0.197E+03	0.623E+01
0.247E+04	0.201E+03	0.565E+01
0.271E+04	0.204E+03	0.327E+01
0.299E+04	0.208E+03	0.479E+01
0.328E+04	0.211E+03	0.586E+01
0.361E+04	0.213E+03	0.570E+01
0.397E+04	0.219E+03	0.706E+01
0.437E+04	0.225E+03	0.890E+01
0.481E+04	0.227E+03	0.894E+01
0.529E+04	0.229E+03	0.779E+01
0.582E+04	0.234E+03	0.848E+01
0.640E+04	0.238E+03	0.884E+01
0.704E+04	0.239E+03	0.912E+01
0.775E+04	0.235E+03	0.948E+01
0.852E+04	0.233E+03	0.108E+02
0.937E+04	0.228E+03	0.118E+02
0.103E+05	0.226E+03	0.112E+02
0.113E+05	0.227E+03	0.101E+02
0.125E+05	0.228E+03	0.104E+02
0.137E+05	0.228E+03	0.926E+01
0.151E+05	0.224E+03	0.624E+01
0.166E+05	0.221E+03	0.418E+01
0.183E+05	0.216E+03	0.521E+01
0.201E+05	0.209E+03	0.766E+01
0.221E+05	0.202E+03	0.102E+02
0.243E+05	0.196E+03	0.103E+02
0.267E+05	0.189E+03	0.970E+01
0.294E+05	0.184E+03	0.700E+01
0.324E+05	0.153E+03	0.303E+02
0.356E+05	0.178E+03	0.397E+02
0.392E+05	0.209E+03	0.242E+02
0.431E+05	0.189E+03	0.241E+02
0.474E+05	0.174E+03	0.113E+02
0.521E+05	0.174E+03	0.108E+02
0.573E+05	0.160E+03	0.290E+02
0.630E+05	0.143E+03	0.437E+02
0.694E+05	0.155E+03	0.415E+02
0.763E+05	0.154E+03	0.338E+02
0.839E+05	0.144E+03	0.338E+02
0.923E+05	0.141E+03	0.280E+02
0.102E+06	0.138E+03	0.269E+02
0.112E+06	0.126E+03	0.295E+02

Table 5. URC26: continued

R (pc)	$V_{\rm rot}$ (km s^{-1})	$\delta V_{\rm rot}$ (km s^{-1})
0.123E+06	0.114E+03	0.319E+02
0.135E+06	0.127E+03	0.581E+02
0.149E+06	0.130E+03	0.637E+02
0.164E+06	0.134E+03	0.564E+02
0.180E+06	0.140E+03	0.334E+02
0.198E+06	0.120E+03	0.298E+02
0.218E+06	0.832E+02	0.255E+02
0.239E+06	0.776E+02	0.276E+02
0.263E+06	0.107E+03	0.333E+02
0.290E+06	0.123E+03	0.227E+02